Ocean Modelling 43-44 (2012) 36–51

Contents lists available at SciVerse ScienceDirect

Ocean Modelling

journal homepage: www.elsevier.com/locate/ocemod

A high-order adaptive time-stepping TVD solver for Boussinesq modeling of breaking waves and coastal inundation

Fengyan Shi [a,*], James T. Kirby [a], Jeffrey C. Harris [b], Joseph D. Geiman [a], Stephan T. Grilli [b]

[a] Center for Applied Coastal Research, University of Delaware, Newark, DE 19716, USA
[b] Department of Ocean Engineering, University of Rhode Island, Narragansett, RI 02882, USA

ARTICLE INFO

Article history:
Received 29 July 2011
Received in revised form 5 December 2011
Accepted 9 December 2011
Available online 17 December 2011

Keywords:
Boussinesq wave model
TVD Riemann solver
Breaking wave
Coastal inundation

ABSTRACT

We present a high-order adaptive time-stepping TVD solver for the fully nonlinear Boussinesq model of Chen (2006), extended to include moving reference level as in Kennedy et al. (2001). The equations are reorganized in order to facilitate high-order Runge–Kutta time-stepping and a TVD type scheme with a Riemann solver. Wave breaking is modeled by locally switching to the nonlinear shallow water equations when the Froude number exceeds a certain threshold. The moving shoreline boundary condition is implemented using the wetting–drying algorithm with the adjusted wave speed of the Riemann solver. The code is parallelized using the Message Passing Interface (MPI) with non-blocking communication. Model validations show good performance in modeling wave shoaling, breaking, wave runup and wave-averaged nearshore circulation.

1. Introduction

Boussinesq wave models have become a useful tool for modeling surface wave transformation from deep water to the swash zone, as well as wave-induced circulation inside the surfzone. Improvements in the range of model applicability have been obtained with respect to classical restrictions to both weak dispersion and weak nonlinearity. Madsen et al. (1991) and Nwogu (1993) demonstrated that the order of approximation in reproducing frequency dispersion effects could be increased using either judicious choices for the form (or reference point) for Taylor series expansions for the vertical structure of dependent variables, or operators effecting a rearrangement of dispersive terms in already-developed model equations. These approaches, combined with use either of progressively higher order truncated series expansions (Gobbi et al., 2000; Agnon et al., 1999) or multiple level representations (Lynett and Liu, 2004), have effectively eliminated the restriction of this class of model to relatively shallow water, allowing for their application to the entire shoaling zone or deeper. At the same time, the use of so-called "fully-nonlinear" formulations (e.g., Wei et al. (1995) and many others) effectively eliminates the restriction to weak nonlinearity by removing the wave height to water depth ratio as a scaling or expansion parameter in the development of approximate governing equations. This approach has improved model applicability in the surf and swash zones particularly, where surface fluctuations are of the order of mean water depth at least and which can represent the total vertical extent of the water column in swash conditions. Representations of dissipative wave-breaking events, which do not naturally arise as weak discontinuous solutions in the dispersive Boussinesq formulation, have been developed usually following an eddy viscosity formulation due to Zelt (1991), and have been shown to be highly effective in describing surf zone wave height decay. The resulting class of models has been shown to be highly effective in modeling wave-averaged surf zone flows over both simple (Chen et al., 2003; Feddersen et al., 2011) and complex (Geiman et al., 2011) bathymetries. Kim et al. (2009) have further extended the formulation to incorporate a consistent representation of boundary layer turbulence effects on vertical flow structure.

Existing approaches to development of numerical implementations for Boussinesq models include a wide range of finite difference, finite volume, or finite element formulations. In this paper, we describe the development of a new numerical approach for the FUNWAVE model (Kirby et al., 1998), which has been widely used as a public domain open-source code since it's initial development. FUNWAVE was originally developed using an unstaggered finite difference formulation for spatial derivatives together with an iterated 4th order Adams–Bashforth–Moulton (ABM) scheme for time stepping (Wei and Kirby, 1995), applied to the fully nonlinear model equations of Wei et al. (1995). In this scheme, spatial differencing is handled using a mixed-order approach, employing fourth-order accurate centered differences for first derivatives and second-order accurate differences for third derivatives. This choice was made in order to move leading order truncation errors to one order higher than the $O(\mu^2)$ dispersive terms (where μ is

* Corresponding author. Tel.: +1 302 831 2449.
E-mail address: fyshi@udel.edu (F. Shi).

1463-5003/$ - see front matter © 2011 Elsevier Ltd. All rights reserved.
doi:10.1016/j.ocemod.2011.12.004

ratio of a characteristic water depth to a horizontal length, a dimensionless parameter characterizing frequency dispersion), while maintaining the tridiagonal structure of spatial derivatives within time-derivative terms. This scheme is straightforward to develop and has been widely utilized in other Boussinesq models. Kennedy et al. (2000) and Chen et al. (2000) describe further aspects of the model system aimed at generalizing it for use in modeling surf zone flows. Breaking is handled using a generalization to two horizontal dimensions of the eddy viscosity model of Zelt (1991). Similar approaches have been used by other Boussinesq model developers, such as Nwogu and Demirbilek (2001), who used a more sophisticated eddy viscosity model in which the eddy viscosity is expressed in terms of turbulent kinetic energy and a length scale. The presence of a moving shoreline in the swash zone is handled using a "slot" or porous-beach method, in which the entire domain remains wetted using a network of slots at grid resolution which are narrow but which extend down to a depth lower than the minimum expected excursion of the modelled free surface. These generalizations form the basis for the existing public domain version of the code (Kirby et al., 1998). Subsequently, several extensions have been made in research versions of the code. Kennedy et al. (2001) improved nonlinear performance of the model by utilizing an adaptive reference level for vertical series expansions, which is allowed to move up and down with local surface fluctuations. Chen et al. (2003) extended the model to include longshore periodic boundary conditions and described it's application to modeling longshore currents on relatively straight coastlines. Shi et al. (2001) generalized the model coordinate system to non-orthogonal curvilinear coordinates. Finally, Chen et al. (2003), Chen (2006) provided revised model equations which correct deficiencies in the representation of higher order advection terms, leading to a set of model equations which, in the absence of dissipation effects, conserve depth-integrated potential vorticity to $O(\mu^2)$, consistent with the level of approximation in the model equations.

The need for a new formulation for FUNWAVE arose from recognition of several crucial problems with the existing code. First, the original model proved to be noisy. or at least weakly unstable to high wavenumbers near the grid Nyquist limit. In addition, both the implementation of the eddy viscosity model for surf zone wave breaking and the interaction of runup with beach slots proved to be additional sources of noise in model calculations. In the original unstaggered grid finite difference scheme, these effects led to the need for periodic application of dissipative filters, with the frequency of filtering increased in areas with active breaking. The overall grid-based noise generation was found to stem from several sources. First, Kennedy et al. (2001, personal communications), during development of a High Performance Fortran (HPF) version of the code on an early linux cluster, discovered that the noise was partially due to implementation of boundary conditions and could be alleviated to an extent. At the same time, the curvilinear model developed by Shi et al. (2001) was implemented using a staggered grid for spatial differencing, and the resulting code was found to be less susceptible to the general grid noise problem. A comparison of noise levels in the original FUNWAVE, the staggered grid scheme of Shi et al., and the corrected boundary condition formulation of Kennedy may be found in Zhen (2004).

Additional sources of noise related either to the eddy viscosity formulation or interaction between the flow and beach "slots" remain less well analyzed or understood. In addition, the performance of the slots themselves has been called into question in several cases involving inundation over complex bathymetry. Slots which are too wide relative to the model grid spacing may admit too much fluid before filling during runup, and cause both a reduction in amplitude and a phase lag in modeled runup events. At the other extreme, slots which are too narrow tend to induce a great deal of numerical noise, leading to the need for intermittent or even fairly frequent filtering of swash zone solutions. Poor model performance in comparison to data for the case of Lynett et al. (2010), described below in Section 4.3, was the determining factor in the decision to pursue a new model formulation.

A number of recently development Boussinesq-type wave models have used a hybrid method combining the finite-volume and finite-difference TVD (Total Variation Diminishing)-type schemes (Toro, 2009), and have shown robust performance of the shock-capturing method in simulating breaking waves and coastal inundation (Tonelli and Petti, 2009, 2010; Roeber et al., 2010; Shiach and Mingham, 2009; Erduran et al., 2005, and others). The use of the hybrid method, in which the underlying components of the nonlinear shallow water equations (which form the basis of the Boussinesq model equations) are handled using the TVD finite volume method while dispersive terms are implemented using conventional finite differencing, provides a robust framework for modeling of surf zone flows. In particular, wave breaking may be handled entirely by the treatment of weak solutions in the shock-capturing TVD scheme, making the implementation of an explicit formulation for breaking wave dissipation unnecessary. In addition, shoreline movement may be handled quite naturally as part of the Reiman solver underlying the finite volume scheme.

In this paper, we describe the development of a hybrid finite volume-finite difference scheme for the fully nonlinear Boussinesq model equations of Chen (2006), extended to incorporate a moving reference level as in Kennedy et al. (2001). The use of a moving reference elevation is more consistent with a time-varying representation of elevation at a moving shoreline in modeling of a swash zone dynamics and coastal inundation. A conservative form of the equations is derived. Dispersive terms are reorganized with the aim of constructing a tridiagonal structure of spatial derivatives within time-derivative terms. The surface elevation gradient term are also rearranged to obtain a numerically well-balanced form, which is suitable for any numerical order. In contrast to previous high-order temporal schemes, which usually require uniform time-stepping, we use adaptive time stepping based on a third-order Runge–Kutta method. Spatial derivatives are discretized using a combination of finite-volume and finite-difference methods. A high-order MUSCL (Monotone Upstream-centered Schemes for Conservation Laws) reconstruction technique, which is accurate up to the fourth-order, is used in the Riemann solver. The wave breaking scheme follows the approach of Tonelli and Petti (2009), who used the ability of the nonlinear shallow water equations (NLSWE) with a TVD solver to simulate moving hydraulic jumps. Wave breaking is modeled by switching from Boussinesq to NSWE at cells where the Froude number exceeds a certain threshold. A wetting–drying scheme is used to model a moving shoreline.

The paper is organized as follows. Section 2 shows derivations of the conservative form of theoretical equations with a well-balanced pressure gradient term. The numerical implementation, including the hybrid numerical schemes, wetting–drying algorithm, boundary conditions and code parallelization, are described in Section 3. Section 4 illustrates four model's applications to problems of wave breaking, wave runup and wave-averaged nearshore circulations. Conclusions are made in Section 5.

2. Fully-nonlinear Boussinesq equations

In this section, we describe the development of a set of Boussinesq equations which are accurate to $O(\mu^2)$ in dispersive effects. Here, μ is a parameter characterizing the ratio of water depth to wave length, and is assumed to be small in classical Boussinesq theory. We retain dimensional forms below but will refer to the

apparent $O(\mu^2)$ ordering of terms resulting from deviations from hydrostatic behavior in order to identify these effects as needed. The model equations used here follow from the work of Chen (2006). In this and earlier works starting with Nwogu (1993), the horizontal velocity is written as

$$\mathbf{u} = \mathbf{u}_\alpha + \mathbf{u}_2(z) \tag{1}$$

Here, $\mathbf{u}_\alpha$ denotes the velocity at a reference elevation $z = z_\alpha$, and

$$\mathbf{u}_2(z) = (z_\alpha - z)\nabla A + \frac{1}{2}(z_\alpha^2 - z^2)\nabla B \tag{2}$$

represents the depth-dependent correction at $O(\mu^2)$, with A and B given by

$$A = \nabla\cdot(h\mathbf{u}_\alpha)$$
$$B = \nabla\cdot\mathbf{u}_\alpha \tag{3}$$

The derivation follows Chen (2006) except for the additional effect of letting the reference elevation z_α vary in time according to

$$z_\alpha = \zeta h + \beta\eta \tag{4}$$

where h is local still water depth, η is local surface displacement and ζ and β are constants, as in Kennedy et al. (2001). This addition does not alter the details of the derivation, which are omitted below.

2.1. Governing equations

The equations of Chen (2006) extended to incorporate a possible moving reference elevation follow. The depth-integrated volume conservation equation is given by

$$\eta_t + \nabla\cdot\mathbf{M} = 0 \tag{5}$$

where

$$\mathbf{M} = H\{\mathbf{u}_\alpha + \bar{\mathbf{u}}_2\} \tag{6}$$

is the horizontal volume flux. $H = h + \eta$ is the total local water depth and $\bar{\mathbf{u}}_2$ is the depth averaged $O(\mu^2)$ contribution to the horizontal velocity field, given by

$$\bar{\mathbf{u}}_2 = \frac{1}{H}\int_{-h}^{\eta}\mathbf{u}_2(z)dz = \left(\frac{z_\alpha^2}{2} - \frac{1}{6}(h^2 - h\eta + \eta^2)\right)\nabla B + \left(z_\alpha + \frac{1}{2}(h-\eta)\right)\nabla A \tag{7}$$

The depth-averaged horizontal momentum equation can be written as

$$\mathbf{u}_{\alpha,t} + (\mathbf{u}_\alpha\cdot\nabla)\mathbf{u}_\alpha + g\nabla\eta + \mathbf{V}_1 + \mathbf{V}_2 + \mathbf{V}_3 + \mathbf{R} = 0 \tag{8}$$

where g is the gravitational acceleration and $\mathbf{R}$ represents diffusive and dissipative terms including bottom friction and subgrid lateral turbulent mixing. $\mathbf{V}_1$ and $\mathbf{V}_2$ are terms representing the dispersive Boussinesq terms given by

$$\mathbf{V}_1 = \left\{\frac{z_\alpha^2}{2}\nabla B + z_\alpha\nabla A\right\}_t - \nabla\left[\frac{\eta^2}{2}B_t + \eta A_t\right] \tag{9}$$

$$\mathbf{V}_2 = \nabla\left\{(z_\alpha - \eta)(\mathbf{u}_\alpha\cdot\nabla)A + \frac{1}{2}(z_\alpha^2 - \eta^2)(\mathbf{u}_\alpha\cdot\nabla)B + \frac{1}{2}[A + \eta B]^2\right\} \tag{10}$$

The form of (9) allows for the reference level z_α to be treated as a time-varying elevation, as suggested in Kennedy et al. (2001). If this extension is neglected, the terms reduce to the form given originally by Wei et al. (1995). The expression (10) for $\mathbf{V}_2$ was also given by Wei et al. (1995), and is not altered by the choice of a fixed or moving reference elevation.

The term $\mathbf{V}_3$ in (8) represents the $O(\mu^2)$ contribution to the expression for $\boldsymbol{\omega}\times\mathbf{u} = \omega\mathbf{i}^z\times\mathbf{u}$ (with $\mathbf{i}^z$ the unit vector in the z direction) and may be written as

$$\mathbf{V}_3 = \omega_0\mathbf{i}^z\times\bar{\mathbf{u}}_2 + \omega_2\mathbf{i}^z\times\mathbf{u}_\alpha \tag{11}$$

where

$$\omega_0 = (\nabla\times\mathbf{u}_\alpha)\cdot\mathbf{i}^z = v_{\alpha,x} - u_{\alpha,y} \tag{12}$$

$$\omega_2 = (\nabla\times\bar{\mathbf{u}}_2)\cdot\mathbf{i}^z = z_{\alpha,x}(A_y + z_\alpha B_y) - z_{\alpha,y}(A_x + z_\alpha B_x) \tag{13}$$

Following Nwogu (1993), z_α is usually chosen in order to optimize the apparent dispersion relation of the linearized model relative to the full linear dispersion in some sense. In particular, the choice $\alpha = (z_\alpha/h)^2/2 + z_\alpha/h = -2/5$ recovers a Padé approximant form of the dispersion relation, while the choice $\alpha = -0.39$, corresponding to the choice $z_\alpha = -0.53h$, minimizes the maximum error in wave phase speed occurring over the range $0 \leqslant kh \leqslant \pi$. Kennedy et al. (2001) showed that allowing z_α to move up and down with the passage of the wave field allowed a greater degree of flexibility in optimizing nonlinear behavior of the resulting model equations. In the examples chosen here, where a great deal of our focus is on the behavior of the model from the break point landward, we adopt Kennedy et al.'s "datum invariant" form

$$z_\alpha = -h + \beta H = (\beta - 1)h + \beta\eta = \zeta h + (1+\zeta)\eta \tag{14}$$

with $\zeta = -0.53$ as in Nwogu (1993) and $\beta = 1 + \zeta = 0.47$. This corresponds in essence to a σ coordinate approach, which places the reference elevation at a level 53% of the total local depth below the local water surface. This also serves to keep the model reference elevation within the actual water column over the entire wetted extent of the model domain.

2.2. Treatment of the surface gradient term

The hybrid numerical scheme requires a conservative form of continuity equation and momentum equations, thus requiring a modification of the leading order pressure term in the momentum equation. A numerical imbalance problem occurs when the surface gradient term is conventionally split into an artificial flux gradient and a source term that includes the effect of the bed slope for a non-uniform bed. To eliminate errors introduced by the traditional depth gradient method (DGM), a so-called surface gradient method (SGM) proposed by Zhou et al. (2001) was adopted in the TVD based-Boussinesq models in the recent literatures. Zhou et al. discussed an example of SGM in 1-D and verified that the slope-source term may be canceled out by part of the numerical flux term associated with water depth, if the bottom elevation at the cell center is constructed using the average of bottom elevations at two cell interfaces. Zhou et al. also showed a 2D application, but without explicitly describing 2D numerical schemes. Although this scheme can be extended into 2D following the same procedure as in 1D, it was found that the 2D extension may not be trivial in terms of the bottom construction for a 2D arbitrary bathymetry. Kim et al. (2008) pointed out that the water depth in the slope-source term should be written in a discretized form rather than the value obtained using the bottom construction, implying that their revised SGM is valid for general 2D applications.

For the higher-order schemes, such as the fourth-order MUSCL-TVD scheme (Yamamoto and Daiguji, 1993; Yamamoto et al., 1998) used in the recent Boussinesq applications, the original SGM and the revised SGM may not be effective in removing the artificial source. This problem was recently noticed by some authors, such as Roeber et al. (2010), who kept a first-order scheme (second-order for normal conditions) for the numerical flux term and the slope-source term in order to ensure a well-balanced solution, without adding noise for a rapidly varying bathymetry. The imbalance problem can be solved by a reformulation of this term in terms of deviations from an unforced but separately specified equilibrium state (see general derivations in Rogers et al., 2003

and recent application in Liang and Marche, 2009). Using this technique, the surface gradient term may be split as

$$gH\nabla\eta = \nabla\left[\frac{1}{2}g(\eta^2+2h\eta)\right] - g\eta\nabla h \tag{15}$$

which is well-balanced for any numerical order for an unforced, still water condition.

2.3. Conservative form of fully nonlinear Boussinesq equations

For Chen's (2006) equations or the minor extension considered here, $H\,\mathbf{u}_\alpha$ can be used as a conserved variable in the construction of a conservative form of Boussinesq equations, but this results in a source term in the mass conservation equation, such as in Shiach and Mingham (2009) and Roeber et al. (2010). An alternative approach is to use $\mathbf{M}$ as a conserved variable in terms of the physical meaning of mass conservation. In this study, we used $\mathbf{M}$, instead of $H\mathbf{u}_\alpha$, in the following derivations of the conservative form of the fully nonlinear Boussinesq equations.

Using $\mathbf{M}$ from (6) together with the vector identity

$$\nabla\cdot(\mathbf{uv}) = \nabla\mathbf{u}\cdot\mathbf{v} + (\nabla\cdot\mathbf{v})\mathbf{u} \tag{16}$$

allows (8) to be rearranged as

$$\mathbf{M}_t + \nabla\cdot\left(\frac{\mathbf{MM}}{H}\right) + gH\nabla\eta = H\{\bar{\mathbf{u}}_{2,t} + \mathbf{u}_\alpha\cdot\nabla\bar{\mathbf{u}}_2 + \bar{\mathbf{u}}_2\cdot\nabla\mathbf{u}_\alpha - \mathbf{V}_1 - \mathbf{V}_2 - \mathbf{V}_3 - \mathbf{R}\} \tag{17}$$

Following Wei et al. (1995), we separate the time derivative dispersion terms in $\mathbf{V}_1$ according to

$$\mathbf{V}_1 = \mathbf{V}'_{1,t} + \mathbf{V}''_1 \tag{18}$$

where

$$\mathbf{V}'_1 = \frac{z_\alpha^2}{2}\nabla B + z_\alpha\nabla A - \nabla\left[\frac{\eta^2}{2}B + \eta A\right] \tag{19}$$

and

$$\mathbf{V}''_1 = \nabla[\eta_t(A+\eta B)] \tag{20}$$

Using (15), (19) and (20), the momentum equation can be rewritten as

$$\begin{aligned}\mathbf{M}_t + \nabla\cdot\left[\frac{\mathbf{MM}}{H}\right] + \nabla\left[\frac{1}{2}g(\eta^2+2h\eta)\right] &= H\left\{\bar{\mathbf{u}}_{2,t} + \mathbf{u}_\alpha\cdot\nabla\bar{\mathbf{u}}_2 + \bar{\mathbf{u}}_2\cdot\nabla\mathbf{u}_\alpha - \mathbf{V}'_{1,t} - \mathbf{V}''_1 - \mathbf{V}_2 - \mathbf{V}_3 - \mathbf{R}\right\} \\ &\quad + g\eta\nabla h\end{aligned} \tag{21}$$

A difficulty usually arises in applying the adaptive time-stepping scheme to the time derivative dispersive terms $\bar{u}_{2,t}$ and $\mathbf{V}'_{1,t}$, which was usually calculated using values stored in several time levels in the previous Boussinesq codes such as in Wei et al. (1995) and Shi et al. (2001). To prevent this, the equation can be re-arranged by merging the time derivatives on the right hand side into the time derivative term on the left hand side, giving

$$\begin{aligned}\mathbf{V}_t + \nabla\cdot\left[\frac{\mathbf{MM}}{H}\right] + \nabla\left[\frac{1}{2}g(\eta^2+2h\eta)\right] &= \eta_t(\mathbf{V}'_1 - \bar{\mathbf{u}}_2) + H(\mathbf{u}_\alpha\cdot\bar{\mathbf{u}}_2 + \bar{\mathbf{u}}_2\cdot\nabla\mathbf{u}_\alpha - \mathbf{V}''_1 - \mathbf{V}_2 - \mathbf{V}_3 - \mathbf{R}) \\ &\quad + g\eta\nabla h\end{aligned} \tag{22}$$

where

$$\mathbf{V} = H(\mathbf{u}_\alpha + \mathbf{V}'_1) \tag{23}$$

In (22) η_t can be calculated explicitly using (5) as in Roeber et al. (2010). Eqs. (5) and (21) are the governing equations solved in this study. As $\mathbf{V}$ is obtained, the velocity $\mathbf{u}_\alpha$ can be found by solving a system of equation with tridiagonal matrix formed by (22), in which all cross-derivatives are moved to the right-hand side of the equation.

3. Numerical schemes

3.1. Compact form of governing equations

We define

$$\begin{aligned}&\mathbf{u}_\alpha = (u, v)\\ &\bar{\mathbf{u}}_2 = (U_4, V_4)\\ &\mathbf{M} = (P, Q) = H[u+U_4, v+V_4]\\ &\mathbf{V}'_1 = (U'_1, V'_1)\\ &\mathbf{V}''_1 = (U''_1, V''_1)\\ &\mathbf{V}_2 = (U_2, V_2)\\ &\mathbf{V} = (\overline{U}, \overline{V}) = H\left[(u+U'_1), (v+V'_1)\right]\end{aligned}$$

The generalized conservative form of Boussinesq equations can be written as

$$\frac{\partial\boldsymbol{\Psi}}{\partial t} + \nabla\cdot\boldsymbol{\Theta}(\boldsymbol{\Psi}) = \mathbf{S} \tag{24}$$

where $\boldsymbol{\Psi}$ and $\boldsymbol{\Theta}(\boldsymbol{\Psi})$ are the vector of conserved variables and the flux vector function, respectively, and are given by

$$\boldsymbol{\Psi} = \begin{pmatrix}\eta\\ \overline{U}\\ \overline{V}\end{pmatrix}, \quad \boldsymbol{\Theta} = \begin{pmatrix} P\mathbf{i} + Q\mathbf{j} \\ \left[\frac{P^2}{H} + \frac{1}{2}g(\eta^2+2\eta h)\right]\mathbf{i} + \frac{PQ}{H}\mathbf{j} \\ \frac{PQ}{H}\mathbf{i} + \left[\frac{Q^2}{H} + \frac{1}{2}g(\eta^2+2\eta h)\right]\mathbf{j}\end{pmatrix} \tag{25}$$

$$\mathbf{S} = \begin{pmatrix}0\\ g\eta\frac{\partial h}{\partial x} + \psi_x + HR_x\\ g\eta\frac{\partial h}{\partial y} + \psi_y + HR_y\end{pmatrix} \tag{26}$$

where

$$\begin{aligned}\psi_x &= \eta_t(U'_1 - U_4)\\ &\quad + H(uU_{4,x} + vU_{4,y} + U_4u_x + V_4u_y - U''_1 - U_2 - U_3)\end{aligned} \tag{27}$$

$$\begin{aligned}\psi_y &= \eta_t(V'_1 - V_4)\\ &\quad + H(uV_{4,x} + vV_{4,y} + U_4v_x + V_4v_y - U''_1 - V_2 - V_3)\end{aligned} \tag{28}$$

The expanded forms of $(U'_1, V'_1), (U''_1, V''_1), (U_2, V_2), (U_3, V_3)$ and (U_4, V_4) can be found in Appendix A. For the term $\mathbf{R}$, the bottom stress is approximated using a quadratic friction equation. For modeling wave-generated nearshore currents such as rip current and alongshore current (Chen et al., 1999, 2003), a Smagorinsky (1963)-like subgrid turbulent mixing algorithm is implemented. The eddy viscosity associated with the subgrid mixing is determined by breaking-induced current field. The detailed formulations can be found in Chen et al. (1999). The Smagorinsky subgrid mixing is used in the model application to predicting wave-averaged nearshore circulation described in Section 4.4.

3.2. Spatial discretization

A combined finite-volume and finite-difference method was applied to the spatial discretization. Following Toro (2009), two basic steps are needed to achieve the spatial scheme. The first step is to use a reconstruction technique to compute values at the cell

interfaces. The second step is to use a local Riemann solver to get numerical fluxes at the cell interfaces.

For the flux terms and the first-order derivative terms, a high-order MUSCL-TVD scheme is implemented in the present model. The high-order MUSCL-TVD scheme can be written in a compact form including different orders of accuracy from the second-to the fourth-order, according to Erduran et al. (2005) who modified Yamamoto et al.'s (1998) fourth-order approach. In x-direction, for example, the combined form of the interface construction can be written as follows:

$$\phi^L_{i+1/2} = \phi_i + \frac{1}{4}\left[(1-\kappa_1)\chi(r)\Delta^*\phi_{i-1/2} + (1+\kappa_1)\chi(1/r)\Delta^*\phi_{i+1/2}\right] \quad (29)$$

$$\phi^R_{i-1/2} = \phi_i - \frac{1}{4}\left[(1+\kappa_1)\chi(r)\Delta^*\phi_{i-1/2} + (1-\kappa_1)\chi(1/r)\Delta^*\phi_{i+1/2}\right] \quad (30)$$

where $\phi^L_{i+1/2}$ is the constructed value at the left-hand side of the interface $i+\frac{1}{2}$ and $\phi^R_{i-1/2}$ is the value at the right-hand side of the interface $i-\frac{1}{2}$. The values of $\Delta^*\phi$ are evaluated as follows:

$$\begin{aligned}
\Delta^*\phi_{i+1/2} &= \Delta\phi_{i+1/2} - \kappa_2\Delta^3\bar{\phi}_{i+1/2}/6\\
\Delta\phi_{i+1/2} &= \phi_{i+1} - \phi_i\\
\Delta^3\bar{\phi}_{i+1/2} &= \Delta\bar{\phi}_{i+3/2} - 2\Delta\bar{\phi}_{i+1/2} + \Delta\bar{\phi}_{i-1/2}\\
\Delta\bar{\phi}_{i-1/2} &= \mathrm{minmod}(\Delta\phi_{i-1/2}, \Delta\phi_{i+1/2}, \Delta\phi_{i+3/2})\\
\Delta\bar{\phi}_{i+1/2} &= \mathrm{minmod}(\Delta\phi_{i+1/2}, \Delta\phi_{i+3/2}, \Delta\phi_{i-1/2})\\
\Delta\bar{\phi}_{i+3/2} &= \mathrm{minmod}(\Delta\phi_{i+3/2}, \Delta\phi_{i-1/2}, \Delta\phi_{i+1/2})
\end{aligned} \quad (31)$$

In (31), minmod represents the Minmod limiter and is given by

$$\mathrm{minmod}(j,k,l) = \mathrm{sign}(j)\max\{0, \min[|j|, 2\ \mathrm{sign}(j)k, 2\ \mathrm{sign}(j)l]\}. \quad (32)$$

κ_1 and κ_2 in (29) and (30) are control parameters for orders of the scheme in the compact form. The complete form with $(\kappa_1,\kappa_2) = (1/3,1)$ is the fourth-order scheme given by Yamamoto et al. (1998). $(\kappa_1,\kappa_2) = (1/3,0)$ yields a third-order scheme, while the second-order scheme can be retrieved using $(\kappa_1,\kappa_2) = (-1,0)$.

$\chi(r)$ in (29) and (30) is the limiter function. The original scheme introduced by Yamamoto et al. (1998) uses the Minmod limiter as used in (31). Erduran et al. (2005) found that the use of the van-Leer limiter for the third-order scheme gives more accurate results. Their finding was confirmed by using the present model in the benchmark tests for wave runup conducted by Tehranirad et al. (2011). The van-Leer limiter can be expressed as

$$\chi(r) = \frac{r+|r|}{1+r} \quad (33)$$

where

$$r = \frac{\Delta^*\phi_{i+1/2}}{\Delta^*\phi_{i-1/2}} \quad (34)$$

The numerical fluxes are computed using a HLL approximate Riemann solver

$$\mathbf{\Theta}(\mathbf{\Psi}^L, \mathbf{\Psi}^R) = \begin{cases} \mathbf{\Theta}(\mathbf{\Psi}^L) & \text{if} \quad s_L \geqslant 0 \\ \mathbf{\Theta}^*(\mathbf{\Psi}^L, \mathbf{\Psi}^R) & \text{if} \quad s_L < 0 < s_R \\ \mathbf{\Theta}(\mathbf{\Psi}^R) & \text{if} \quad s_R \leqslant 0 \end{cases} \quad (35)$$

where

$$\mathbf{\Theta}^*(\mathbf{\Psi}^L, \mathbf{\Psi}^R) = \frac{s_R\mathbf{\Theta}(\mathbf{\Psi}^L) - s_L\mathbf{\Theta}(\mathbf{\Psi}^R) + s_Ls_R(\mathbf{\Psi}^R - \mathbf{\Psi}^L)}{s_R - s_L} \quad (36)$$

The wave speeds of the Riemann solver are given by

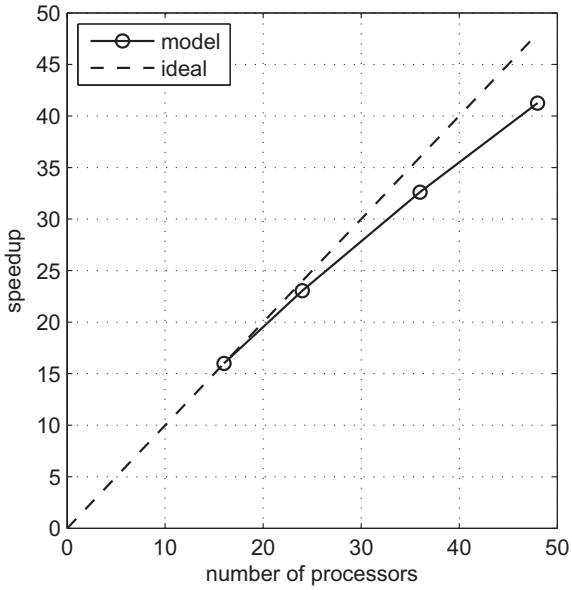

Fig. 1. Variation in model performance with number of processors for a 1800×1800 domain. Straight line indicates arithmetic speedup. Actual performance is shown in the curved line.

$$s_L = \min(\mathbf{V}^L\cdot\mathbf{n} - \sqrt{g(h+\eta)^L}, u_s - \sqrt{\varphi_s}), \quad (37)$$

$$s_R = \max(\mathbf{V}^R\cdot\mathbf{n} + \sqrt{g(h+\eta)^R}, u_s + \sqrt{\varphi_s}), \quad (38)$$

in which u_s and φ_s are estimated as

$$u_s = \frac{1}{2}(\mathbf{V}^L + \mathbf{V}^R)\cdot\mathbf{n} + \sqrt{g(\eta+h)^L} - \sqrt{g(\eta+h)^R} \quad (39)$$

$$\sqrt{\varphi_s} = \frac{\sqrt{g(\eta+h)^L} + \sqrt{g(\eta+h)^R}}{2} + \frac{(\mathbf{V}^L - \mathbf{V}^R)\cdot\mathbf{n}}{4} \quad (40)$$

and $\mathbf{n}$ is the normalized side vector for a cell face.

Higher derivative terms in ψ_x and ψ_y were discretized using a central difference scheme at the cell centroids, as in Wei et al. (1995). No discretization of dispersion terms at the cell interfaces is needed due to using $\mathbf{M}$ as a flux variable. The Surface Gradient Method (Zhou et al., 2001) was used to eliminate unphysical oscillations. Because the pressure gradient term is re-organized as in Section 2.2, there is no imbalance issue for the high-order MUSCL scheme.

3.3. Time stepping

The third-order Strong Stability-Preserving (SSP) Runge–Kutta scheme for nonlinear spatial discretization (Gottlieb et al., 2001) was adopted for time stepping. The scheme is given by

$$\begin{aligned}
\mathbf{\Psi}^{(1)} &= \mathbf{\Psi}^n + \Delta t(-\nabla\cdot\mathbf{\Theta}(\mathbf{\Psi}^n) + \mathbf{S}^{(1)})\\
\mathbf{\Psi}^{(2)} &= \frac{3}{4}\mathbf{\Psi}^n + \frac{1}{4}\left[\mathbf{\Psi}^{(1)} + \Delta t\left(-\nabla\cdot\mathbf{\Theta}(\mathbf{\Psi}^{(1)}) + \mathbf{S}^{(2)}\right)\right]\\
\mathbf{\Psi}^{n+1} &= \frac{1}{3}\mathbf{\Psi}^n + \frac{2}{3}\left[\mathbf{\Psi}^{(2)} + \Delta t\left(-\nabla\cdot\mathbf{\Theta}(\mathbf{\Psi}^{(2)}) + \mathbf{S}^{n+1}\right)\right]
\end{aligned} \quad (41)$$

in which $\mathbf{\Psi}^n$ denotes $\mathbf{\Psi}$ at time level n. $\mathbf{\Psi}^{(1)}$ and $\mathbf{\Psi}^{(2)}$ are values at intermediate stages in the Runge–Kutta integration. As $\mathbf{\Psi}$ is obtained at each intermediate step, the velocity (u,v) can be solved by a system of tridiagonal matrix equations formed by (22). $\mathbf{S}$ needs to be updated using (u,v,η) at the corresponding time step and an iteration is needed to achieve convergence.

An adaptive time step is chosen, following the Courant–Friedrichs–Lewy (CFL) criterion:

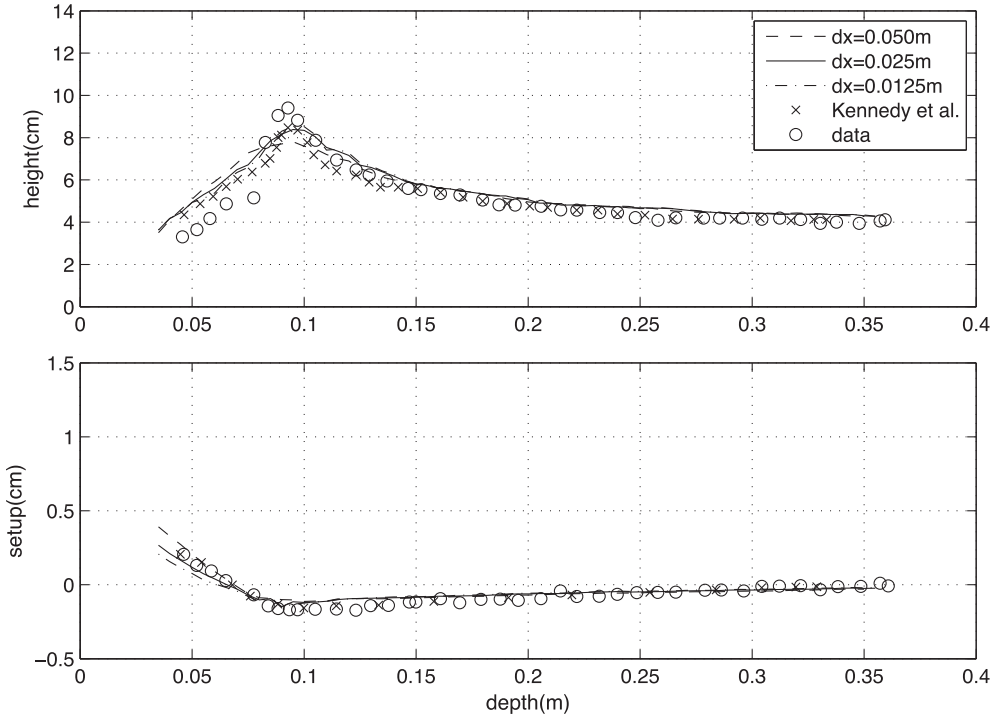

Fig. 2. Comparisons of wave height (upper panel) and wave setup (lower panel) between measured data and model results for a plunging breaker case of Hansen and Svendsen (1979) with grid resolutions of dx = 0.0125 m (dash-dot line), 0.025 m (solid line) and 0.050 m (dashed line). The results of Kennedy et al. (2000) are also shown for comparison (crosses).

$$\Delta t = C \min\left(\min \frac{\Delta x}{|u_{i,j}| + \sqrt{g(h_{i,j}+\eta_{i,j})}}, \min \frac{\Delta y}{|v_{i,j}| + \sqrt{g(h_{i,j}+\eta_{i,j})}}\right) \tag{42}$$

where C is the Courant number. $C = 0.5$ was used in the following examples.

3.4. Wave breaking and wetting–drying schemes for shallow water

The wave breaking scheme follows the approach of Tonelli and Petti (2009), who successfully used the ability of NSWE with a TVD scheme to model moving hydraulic jumps. Thus, the fully nonlinear Boussinesq equations are switched to NSWE at cells where the Froude number exceeds a certain threshold. Following Tonelli and Petti, the ratio of surface elevation to water depth is chosen as the criterion to switch from Boussinesq to NSWE. That means that all dispersive terms, $\mathbf{V}_1'$ in (23) and ϕ_x and ϕ_y in (26) are zero at grid points where the wave is breaking. The threshold value was set to 0.8 in all model tests in Section 4 according to model validations against experimental data, which is also consistent with Tonelli and Petti (2009).

The wetting–drying scheme for modeling a moving boundary is straightforward. The normal flux $\mathbf{n}\cdot\mathbf{M}$ at the cell interface of a dry cell is set to zero. A mirror boundary condition is applied to the fourth-order MUSCL-TVD scheme and discretization of dispersive terms in ψ_x, ψ_y at dry cells. It may be noted that the wave speeds of the Riemann solver (37) and (38) for a dry cell are modified as

$$\begin{aligned} s_L &= \mathbf{V}^L\cdot\mathbf{n} - \sqrt{g(h+\eta)^L}, \\ s_R &= \mathbf{V}^L\cdot\mathbf{n} + 2\sqrt{g(h+\eta)^L} \quad \text{(right dry cell)} \end{aligned} \tag{43}$$

and

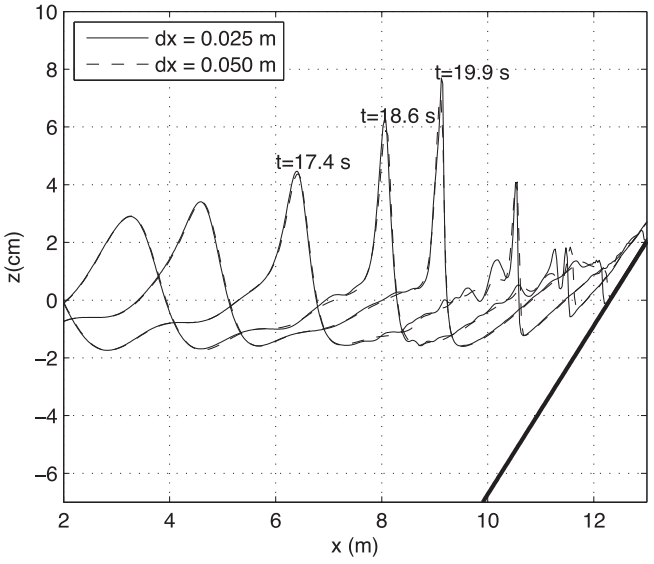

Fig. 3. Snapshots of surface elevation at t = 17.4, 18.6 and 19.9 s from models with grid resolutions of dx = 0.025 (solid lines) and 0.050 m (dashed lines).

$$\begin{aligned} s_L &= \mathbf{V}^R\cdot\mathbf{n} - \sqrt{g(h+\eta)^R}, \\ s_R &= \mathbf{V}^R\cdot\mathbf{n} + 2\sqrt{g(h+\eta)^R} \quad \text{(left dry cell)} \end{aligned} \tag{44}$$

3.5. Boundary conditions and wavemaker

We implemented various boundary conditions including wall boundary condition, absorbing boundary condition following Kirby

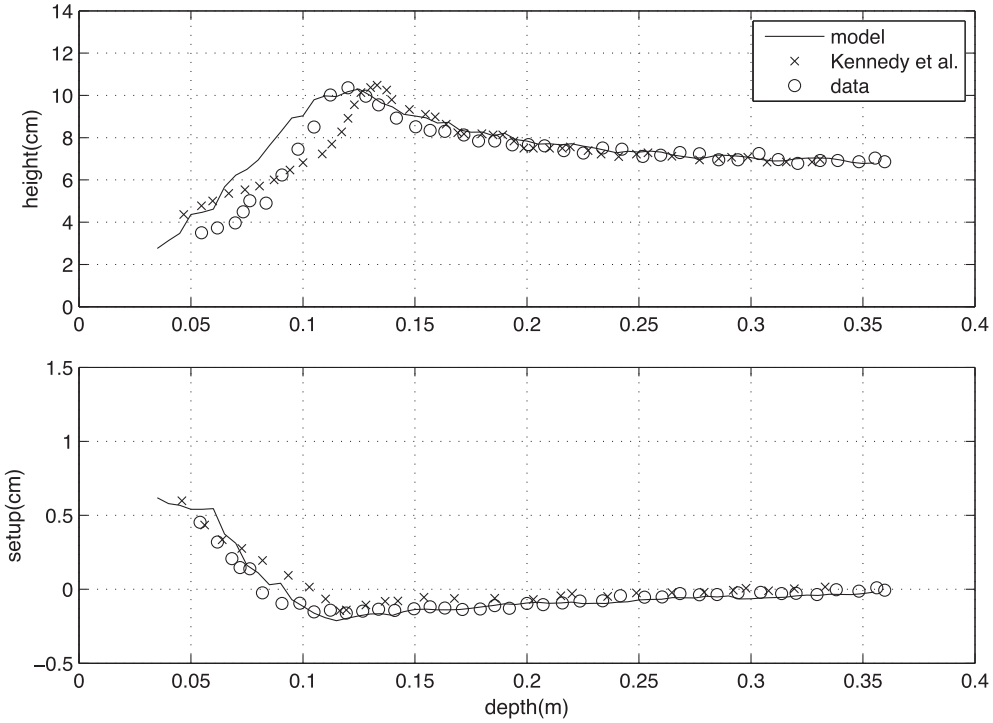

Fig. 4. Model/data comparisons of wave height (upper panel) and wave setup (lower panel) for grid resolution dx = 0.025 m. Spilling breaker case from Hansen and Svendsen (1979). Solid line-present model; x's- Kennedy et al. (2000), eddy viscosity model.

et al. (1998) and periodic boundary condition following Chen et al. (2003).

Wavemakers implemented in this study include Wei et al.'s (1999) internal wavemakers for regular waves and irregular waves. For the irregular wavemaker, an extension was made to incorporate alongshore periodicity into wave generation, in order to eliminate a boundary effect on wave simulations. The technique exactly follows the strategy in Chen et al. (2003), who adjusted the distribution of wave directions in each frequency bin to obtain alongshore periodicity. This approach is effective in modeling of breaking wave-induced nearshore circulation such as alongshore currents and rip currents.

3.6. Parallelization

In parallelizing the computational model, we used a domain decomposition technique to subdivide the problem into multiple regions and assign each subdomain to a separate processor core. Each subdomain region contains an overlapping area of ghost cells three-row deep, as required by the fourth order MUSCL-TVD scheme. The Message Passing Interface (MPI) with non-blocking communication is used to exchange data in the overlapping region between neighboring processors. Velocity components are obtained from Eq. (22) by solving tridiagonal matrices using the parallel pipelining tridiagonal solver described in Naik et al. (1993).

To investigate performance of the parallel program, numerical simulations of an idealized case are tested with different numbers of processors on the Linux cluster Chimera located at University of Delaware. The test case is set up in a numerical grid of 1800 × 1800 cells. Fig. 1 shows the model speedup versus number of processors. It can be seen that performance scales nearly proportional to the number of processors, with some delay caused by inefficiencies in parallelization, such as inter-processor communication time. Chimera nodes consist of 48 cores, so the present simulations on 48 or less cores do not test inter-node communication performance on the system.

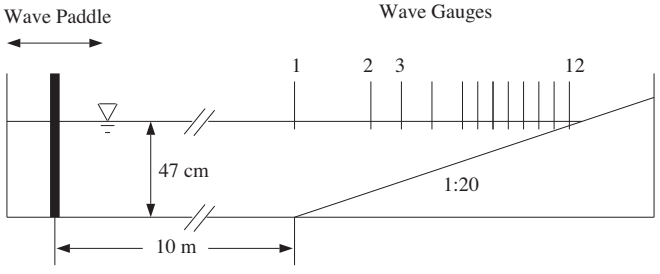

Fig. 5. Experiment layout of Mase and Kirby (1992).

4. Model tests

The model has been validated extensively using laboratory experiments for wave shoaling and breaking, as described in the FUNWAVE manual by Kirby et al. (1998), and a suite of benchmark tests for wave runup. The interested reader is referred to Shi et al. (2011) and Tehranirad et al. (2011). In this paper, we will present four test cases, with a focus on examining the shock-capturing scheme for modeling wave breaking, the wetting–drying algorithm for wave runup, and the model capability in predicting wave-induced nearshore circulation. The fourth-order scheme of Yamamoto et al. (1998) is used in all the test cases. The effect of using adaptive time stepping is demonstrated in the wave runup case.

4.1. Breaking waves on a beach

Hansen and Svendsen (1979) carried out laboratory experiments of wave shoaling and breaking on a beach. Waves were generated on a flat bottom a 0.36 m depth, and the beach slope was 1:34.26. The experiments included several cases including

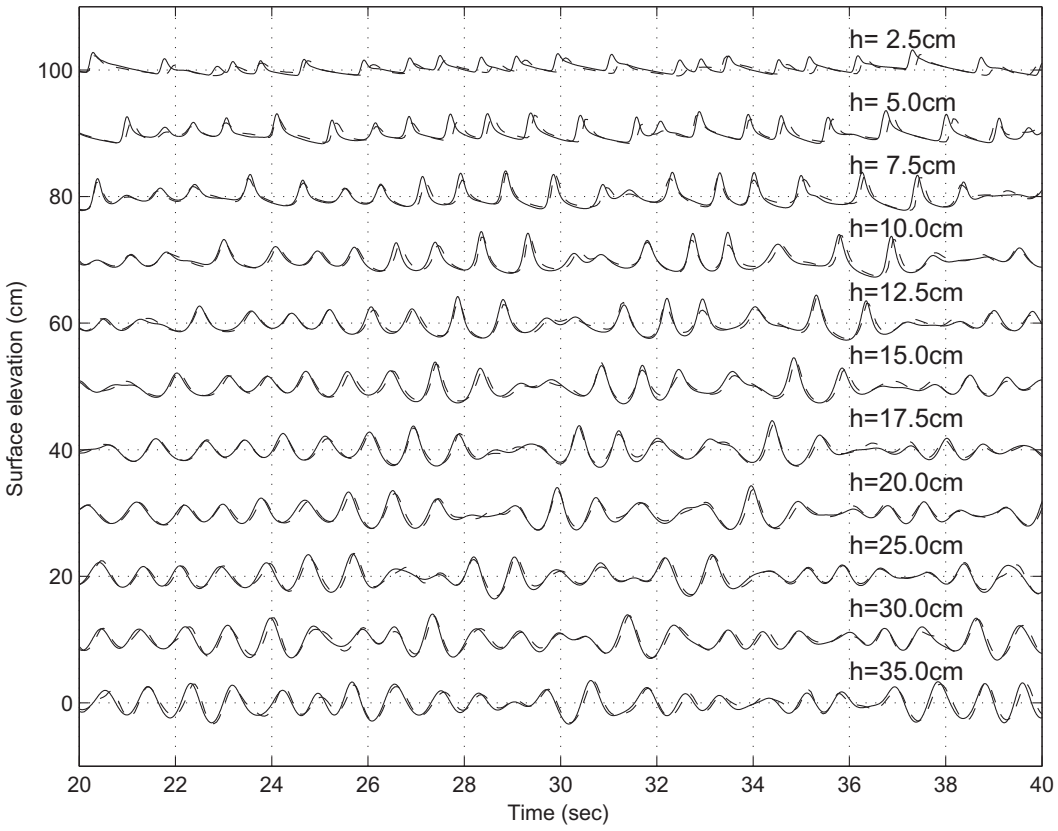

Fig. 6. Time series comparison of η for model (dashed lines) and data (solid lines) at 11 wave gauges in Mase and Kirby (1992).

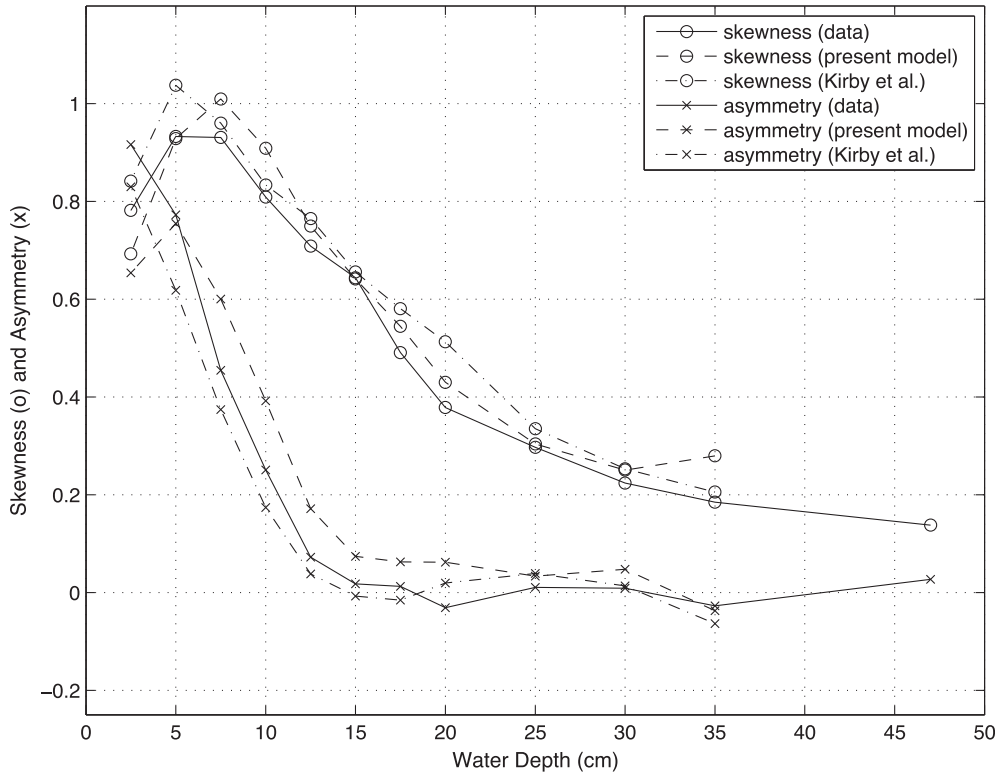

Fig. 7. Comparison of skewness (○) and asymmetry (×) at different water depths. Solid lines are experiment data (Mase and Kirby, 1992). Dashed lines are numerical results for eddy viscosity model (Kirby et al., 1998) and dash-dot lines are results for present model.

plunging breakers, plunging-spilling breakers and spilling breakers. In this paper, we simulate two typical cases: a plunging breaker and a spilling breaker, respectively. The wave height and wave period are 4.3 cm and 3.33 s, respectively, for the plunging case, and 6.7 cm and 1.67 s for the spilling case.

Although the shock-capturing breaking algorithm used in Boussinesq wave models has been examined by previous researchers (e.g., Tonelli and Petti, 2009; Shiach and Mingham, 2009 and others), there is a concern about its sensitivity to grid spacing. Erduran et al. (2005) discussed numerical diffusivity caused by several types of limiters in a TVD scheme. In this study, we intended to examine the grid spacing effect on prediction of breaking wave height. We adopted three grid sizes, dx = 0.05 m, 0.025 m and 0.0125 m, respectively, for each cases. Fig. 2 shows comparisons of wave height and wave setup between measured data and numerical results from model runs with different grid sizes. Results from the previous version of FUNWAVE with the same breaking parameters as in Kennedy et al. (2000) are also plotted in the figure for comparison. The wave breaking location of wave setup/setdown predicted by the three runs are in agreement with the data, however, the predicted maximum wave heights are slightly different. Results from dx = 0.025 m and 0.0125 m grids are very close, indicating a convergence with grid refinement. All three models underpredict the peak wave height at breaking and overpredict wave height inside of the surfzone. This prediction trend was also found in Kennedy et al. (2000) as shown in the figure. 10% and 9.2% underpredictions of peak wave height can be found in the tests with dx = 0.025 m and 0.0125 m, respectively, while Kennedy et al. (2000) underpredicted the peak wave height by 10% with dx = 0.02 m. The present model with a coarser grid (dx = 0.05 m) underpredicted the peak wave height by 17%. Numerical errors for wave height prediction over all measurement locations were estimated using the relative root-mean-square-error (RMSE) normalized by the measured maximum wave height. The relative RMSEs for dx = 0.050, 0.025 and 0.0125 m are 8.2%, 6.8% and 6.0%, respectively. For predictions of wave setup/set down, the relative RMSE was normalized by the range of setup/set down. They are 10.8%, 9.6% and 9.0%, respectively, for dx = 0.050, 0.025 and 0.0125 m.

To find the cause of the large underprediction of peak wave height in the coarser grid model, in Fig. 3, we show snapshots of surface elevation from model results with dx = 0.025 m and 0.050 m at different times. The model with the finer grid resolution switched from the Boussinesq equations to NSWE around t = 19.9 s (the model with the coarser grid switched slightly later) at the point where the ratio of surface elevation to water depth reached the threshold value of 0.8. Then, a wave is damped at the sharp front and generates trailing high frequency oscillations. The comparison of wave profiles at an early time (i.e. t = 18.6 s) shows that the coarser grid model underpredicts wave height before the Boussinesq-NSWE switching, indicating that the underprediction is not caused by the shock-capturing scheme, but by the numerical dissipation resulting from the coarse grid resolution.

It should be mentioned that there is a discontinuity at the point switching between the Boussinesq equations and NSWE, as pointed by one of reviewers. The discontinuity is expected to be small as kh is small in shallow water. In the present case, for example, a switch occurs at kh = 0.38, where the ratio of dispersive wave phase speed to non-dispersive phase speed ($\sqrt{gh}$) is 0.98.

For the spilling breaker case, the models with three different grid sizes basically predicted slightly different wave peaks as in the plunging wave case. Fig. 4 shows results from dx = 0.25 m, with comparisons to measured data and Kennedy et al.'s (2000) results. The relative RMSEs for wave height prediction are 8.5% from the present model and 7.4% from Kennedy et al. (2000). The relative RMSE's for wave setup/set down prediction are 8.5% and 13.0%, respectively, from the present model and Kennedy et al.

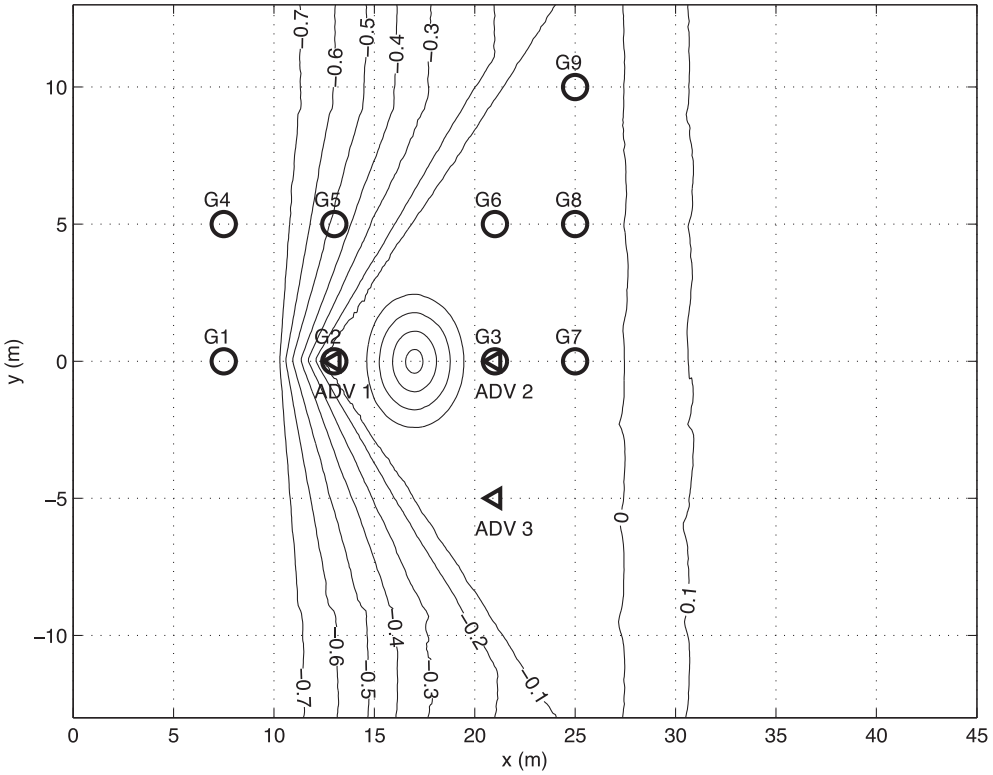

Fig. 8. Bathymetry contours (in meters) and measurement locations used in model simulations for OSU tank bathymetry (Lynett et al., 2010). Circles: pressure gauges, triangles: ADV.

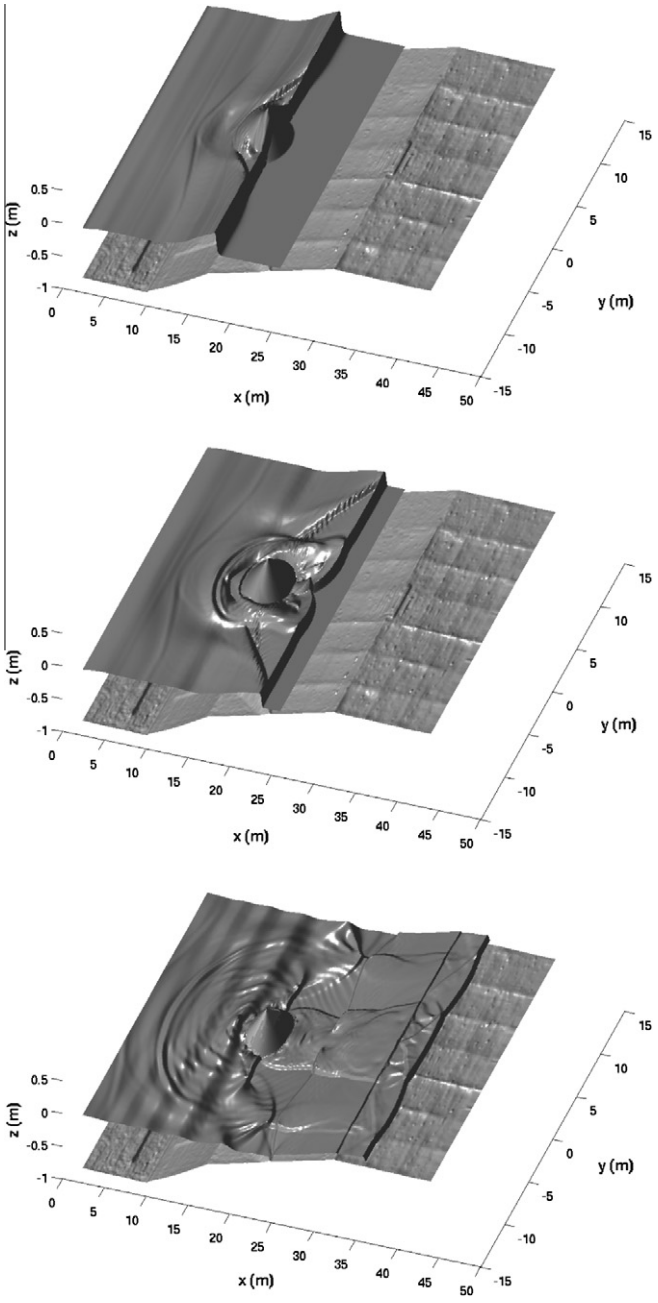

Fig. 9. Modeled water surface at (top) t = 6.4 s, (middle) t = 8.4 s, (bottom) t = 14.4 s.

4.2. Irregular wave shoaling and breaking on a slope

To study irregular-wave properties during shoaling and breaking, Mase and Kirby (1992) conducted a laboratory experiment for random wave propagation over a planar beach. The experimental layout is shown in Fig. 5, where a constant depth of 0.47 m on the offshore side connects to a constant slope of 1:20 on the right. Two sets of random waves with peak frequencies of 0.6 Hz (run 1) and 1.0 Hz (run 2) were generated by the wavemaker on the offshore side. The target incident spectrum was a Pierson–Moskowitz spectrum. Wave gauges collected time series of surface elevation at depths h = 47, 35, 30, 25, 20, 17.5, 15, 12.5, 10, 7.5, 5, and 2.5 cm.

The present case has been previously studied using an eddy viscosity model for breaking waves by Kennedy et al. (2000). The present model was set up following Kennedy et al. (2000), who used an internal wavemaker located at the toe of the slope, where

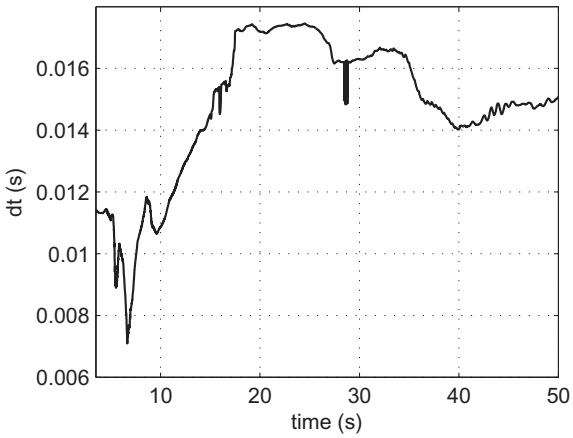

Fig. 10. Time step variation.

surface elevation is measured by gauge 1. The internal wavemaker signal was constructed following Wei et al. (1999), using low and high-frequency cutoffs of 0.2 Hz and 10.0 Hz. The simulation time is the same as the time length of data collection. The computational domain extends from x = 0 m to 20 m, with a grid size of 0.04 m. The toe of the slope starts at x = 10 m. A sponge layer is specified at the offshore side boundary, to absorb reflected waves, but no sponge layer is needed on the onshore boundary, which differs from Kirby et al. (1998) who used the slot method combined with a sponge layer at the end of the domain.

We present the model results for run 2 and compare them with the experimental data measured at the other 11 gauges shown in Fig. 5. Fig. 6 shows model results (dashed lines) and measured data (solid lines) from t = 20 s to t = 40 s at those gauges. Both model and data show that most waves start breaking at a h = 15 cm depth. Except for small discrepancies in wave phases, the model reproduces the measured waveform quite well. The standard deviation of the predicted surface elevation are calculated at all 11 gauges and compared to the data. The relative computational errors are between 0.4 $\sim$ 7.5%. The relative RMSE of standard deviation calculated over the 11 gauges is 5.4%.

Third moment statistics of surface elevation provide a good evaluation of model skill in reproducing wave crest shape. Normalized wave skewness and asymmetry were calculated for both measured and modeled time series of surface elevation according to the following formulations,

$$\begin{aligned} \text{skew} &= \frac{\langle \eta^3 \rangle}{\langle \eta^2 \rangle^{3/2}} \\ \text{asym} &= \frac{\langle H(\eta)^3 \rangle}{\langle \eta^2 \rangle^{3/2}} \end{aligned} \tag{45}$$

where H denotes the Hilbert transform, $\langle\rangle$ is the time-averaging operator, and the mean has been removed from the time series of surface elevation.

Fig. 7 shows the skewness and asymmetry predicted by the present model, the original FUNWAVE (Kirby et al., 1998) and experiment data. We see, the both models predicted skewness and asymmetry reasonably well, with a slight overprediction of wave skewness inside the surf zone. The relative RMSE for skewness prediction, which is normalized by the measured maximum value, is 6.6% from the present model and 7.1% for Kirby et al. The relative RMSEs for asymmetry prediction are 12.1% and 7.4% from the present model and Kirby et al., respectively.

It is worth mentioning that Kirby et al. (1998) employed frequent use of numerical filtering, especially after wave breaking, so that the model run was stable over the entire data time series.

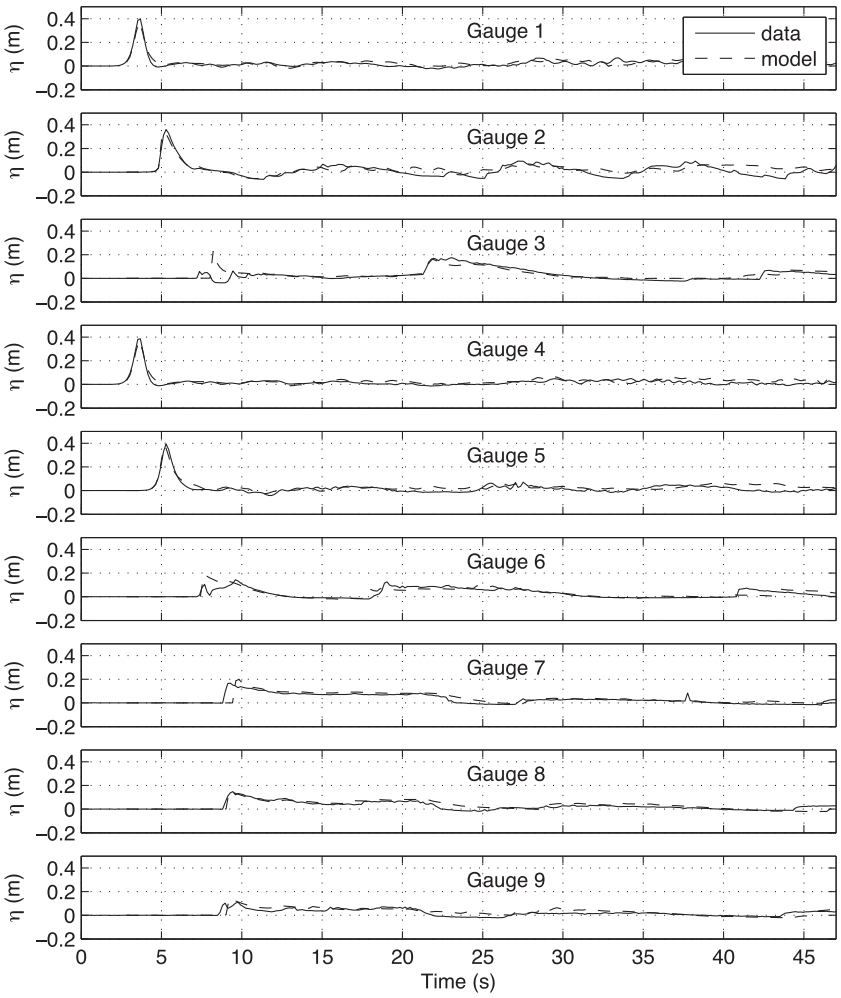

Fig. 11. Model/data comparisons of time series of surface elevation at (top) Gauge 1–Gauge 9. Solid line: model, dashed line: data.

The present model did not encounter any stability problem and utilizes no filtering.

4.3. Solitary wave runup on a shelf with a conical island

To examine the wetting–drying method used in the present model versus the slot method used in Kennedy et al. (2000), Chen et al. (2000), we performed a simulation of the solitary wave runup measured recently in a large wave basin at Oregon State University's O.H. Hinsdale Wave Research Laboratory (Lynett et al., 2010). The basin is 48.8 m long, 26.5 m wide, and 2.1 m deep. A complex bathymetry consisting of a 1:30 slope planar beach connected to a triangle shaped shelf and a conical island on the shelf was used and is shown in Fig. 8. Solitary waves were generated on the left side by a piston-type wavemaker. Surface elevation and velocity were collected at many locations by wave gauges and ADV's in alongshore and cross-shore arrays. Fig. 8 shows wave gauges (circles) and ADV's (triangles) used for model/data comparisons in the present study. Gauge 1–9 were located at (x,y) = (7.5, 0.0) m, (13.0, 0.0) m, (21.0, 0.0) m, (7.5, 5.0) m, (13.0, 5.0) m, (21.0, 5.0) m, (25.0, 0.0) m, (25.0, 5.0) m and (25.0, 10.0) m, respectively. ADV 1–3 were located at (13.0, 0.0) m, (21.0, 0.0) m and (21.0, −5.0) m, respectively.

The modeled bathymetry was constructed by combining the measured data of the shelf and the analytical equation of the cone, which was used for the design of the island in the experiment. The computational domain was modified by extending the domain from x = 0.0 m to −5.0 m with a constant water depth of 0.78 m in order to use a solitary wave solution as an initial condition. The width of the computational domain in the y direction is the same as OSU's basin. Grid spacing used in the model is 0.1 m in both directions. A solitary wave solution based on Nwogu's extended Boussinesq equations (Wei, 1997) was used with centroid located at x = 5.0 m at time t = 0 s. The wave height is 0.39 m, as used in the laboratory experiment.

Fig. 9 shows results of computed water surfaces at t = 6.4 s, 8.4 s and 14.4 s, respectively. The wave front becomes very steep as the wave climbs on the shelf, which was well captured by the model. The wave scattering pattern is clearly seen in the bottom panel of Fig. 9. Wave breaking on the shelf was observed in the laboratory experiment and was also seen in the model. Fig. 10 shows the variation in time stepping during the simulation. The time step dropped to a minimum, at around t = 6.5 s, as the wave collided with the island (top panel of Fig. 9). The local Froude number reached a maximum at t = 6.5 s, reducing the value of the time step based on (42).

Fig. 11 shows time series of modeled surface elevations and measurements at Gauge 1–9 (from top to bottom). Good agreement between model and data is found at the gauge in front of the island (Gauge 1, top panel), as the model successfully predicts the solitary wave propagation and its reflection from the shore. The model also captures the collision of edge waves propagating around the two sides of the island, as indicated at the gauge behind the island (Gauge 3). The model predicts the timing of wave

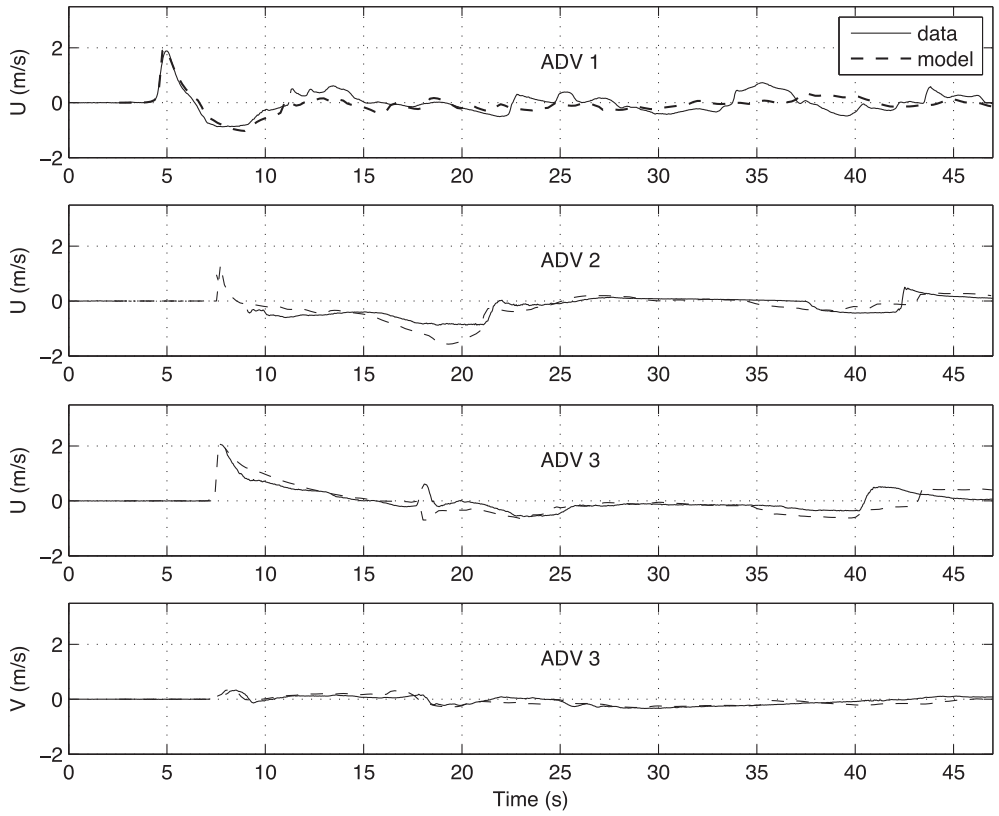

Fig. 12. Model/data comparisons of time series of velocity u component at ADV 1 (top panel), ADV 2 (second panel), ADV 3 (third panel), and v component at ADV 3 (bottom panel). Solid line: model, dashed line: data.

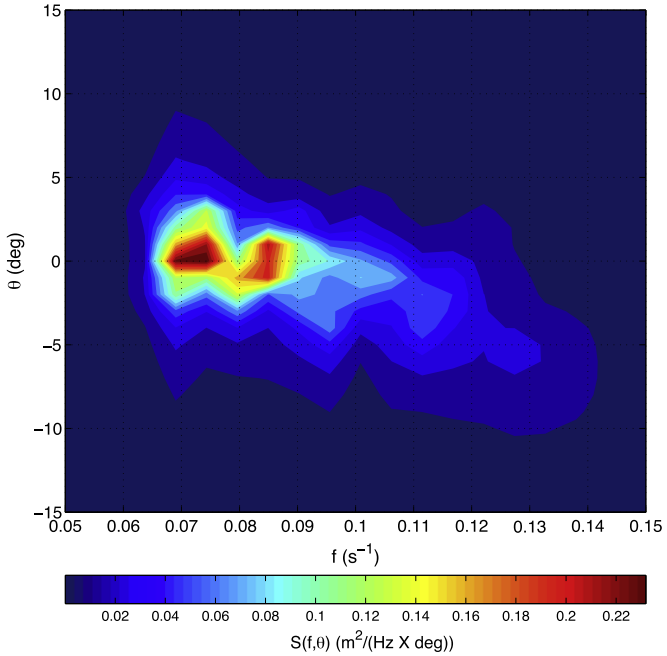

Fig. 13. Wave spectrum $S(f,\theta)$ in $m^2/(Hz \times deg)$ from the offshore ADCP at 13 m water depth, averaged over the entire yearday 124. θ has been rotated so that the shore normal direction is $\theta = 0^\circ$ and positive values represent northward.

collision well but over-predicts the peak of wave runup. The model/data comparisons at Gauges 5, 6, 8, and 9, which are located at the north-side shelf, indicates that the model predicts wave refraction and breaking on the shelf reasonably well. The averaged RMSE normalized by the maximum measured wave amplitude is 7.5% with the maximum RMSE of 11.2% at Gauge 2 and the minimum RMSE of 3.7% at Gauge 1.

Fig. 12 shows model/data comparisons of velocity time series of velocity u component at ADV 1 (top panel), ADV 2 (second panel), ADV 3 (third panel), and v component at ADV 3 (bottom panel). The model predicts the peak velocity and the entire trend of velocity variation in time at measurement locations. An underprediction of the seaward velocity is found at ADV 2. The velocity in the y-direction was not compared at ADV 1 and ADV2 because the measured values were too small. The relative RMSEs calculated at ADV 1 and ADV 2 are 10.5% and 14.8%, respectively. The relative RMSE at ADV 3 is 9.3% for u prediction and 20.0% for v prediction.

4.4. Wave-averaged nearshore circulation

Boussinesq models have been used to model rip currents (Chen et al., 1999; Johnson and Pattiaratchi, 2006; Geiman et al., 2011) and alongshore currents (Chen et al., 2003; Feddersen et al., 2011) in field surfzone situations. Recently, Feddersen et al. (2011) compared results of waves and currents from the Boussinesq model FUNWAVE-C with observations during five surfzone dye release experiments. The comparisons indicated that the Boussinesq model reproduced well the observed cross-shore evolution of significant wave height, mean wave angle, bulk directional spread, mean alongshore current, and the frequency-dependent sea-surface elevation spectra and directional moments. Geiman et al. (2011) conducted a numerical study on wave averaging effects on estimates of the surfzone mixing, using the phase-resolving Boussinesq model FUNWAVE and the wave averaged model Delft3D. Results from both models were compared to field observation at the RCEX field experiment (Brown et al., 2009; MacMahan et al., 2010). Their study showed that each model is able to

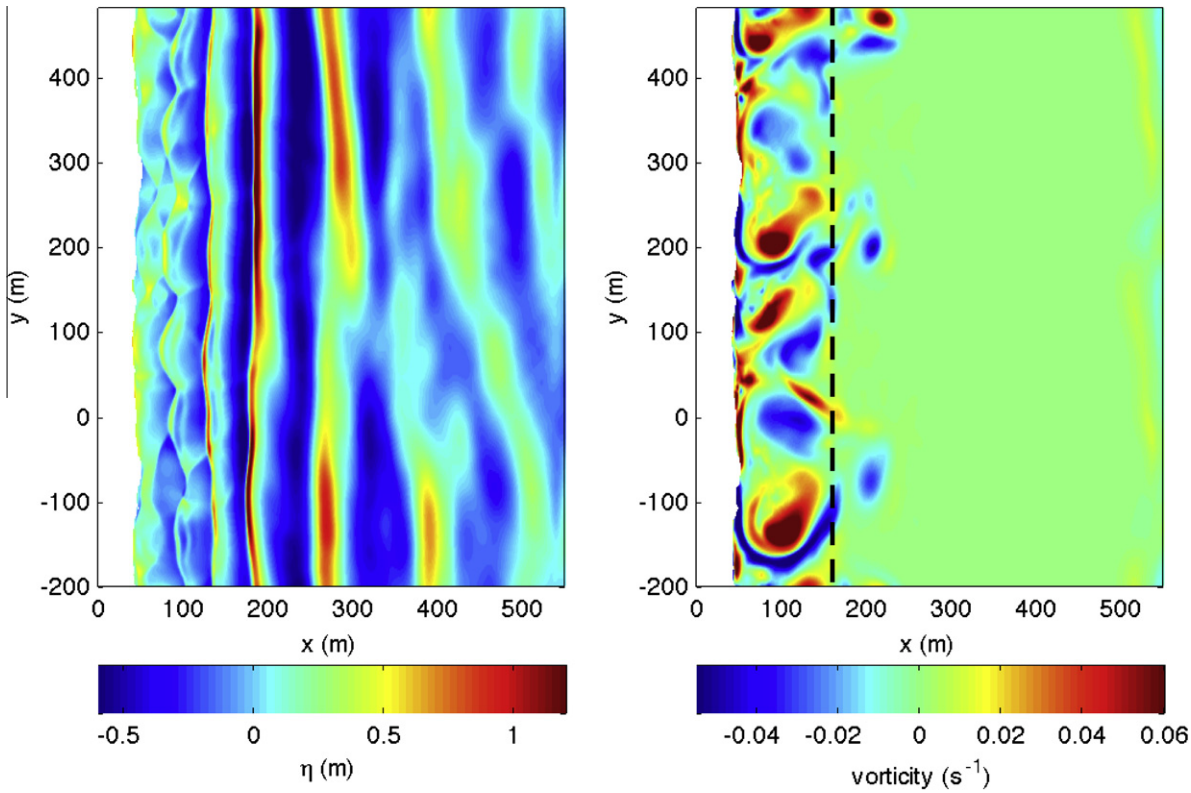

Fig. 14. Snapshots of wave surface elevation field (left panel) and vorticity field (right panel). The dashed line represents the approximate outer limit of the surfzone.

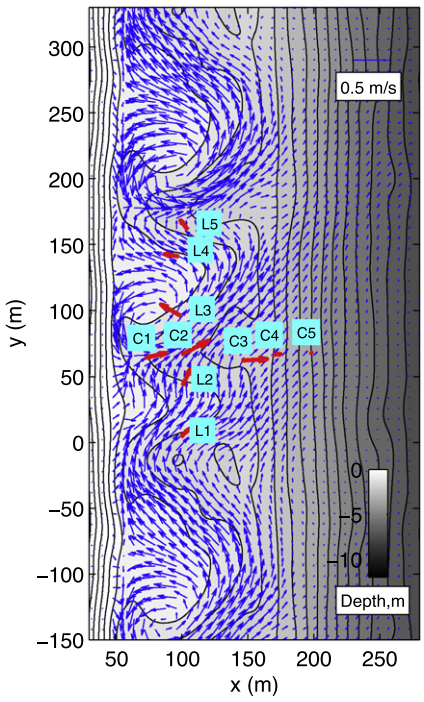

Fig. 15. Modeled wave-averaged current field (blue arrows) and measured wave-averaged current velocities (red arrows). Water depth contours are black lines and locations of in situ instrumentation are marked in text (C1–C5 represent the across-shore array and L1–L5 are the alongshore array.) (For interpretation of the references to colour in this figure legend, the reader is referred to the web version of this article.)

reproduce 1-h time-averaged mean Eulerian velocities consistent with field measurements at stationary current meters. However, the spatial distribution of wave height inside the surfzone was different between the two models, due to the different mechanisms for wave breaking.

To check the breaking scheme used in the present model and its consequences regarding wave-induced currents, we set up the present model in the same way as in Geiman et al. (2011), except that no sponge layer was applied for the present model at the shoreline position. The model used a grid size of $dx = dy = 1$ m and a north–south periodic boundary condition in a computational domain of 732 m $\times$ 684 m. An internal wavemaker for directional irregular wave generation was located at 540 m away from the shoreline. The directional spectra observed at 13 m water depth during the instrument deployment was divided into 23 $\times$ 31 bins as shown in Fig. 13. The calculated RMS wave height $H_{rms} = 0.65$ m and period $T_{mo} = 10.5$ s.

Snapshots of model sea-surface elevation and vorticity are shown in Fig. 14. Waves approach the beach in a closely shore-normal direction with narrow directional spreading, as expected based on the wave spectrum input. Breaking wave-generated vortices are mostly confined to the surfzone as shown in the right panel of Fig. 14.

Fig. 15 shows wave-averaged currents calculated by 1-h averaging over modeled (u_α, v_α). The red arrows show the wave-averaged velocities observed at measurement locations, L1–L5 in the alongshore array and C1–C5 in the cross-shore array. The model shows a good agreement with the data. Both the model and the data indicate that the mean circulation pattern is tied to the rip channels.

Fig. 16 shows the comparison between the RMS wave height calculated from the model at $y = 65$ m and the data (circles) at the measurement locations C1, C2, C4 and C5, marked in Fig. 15. A fairly good agreement is obtained in the model/data comparison

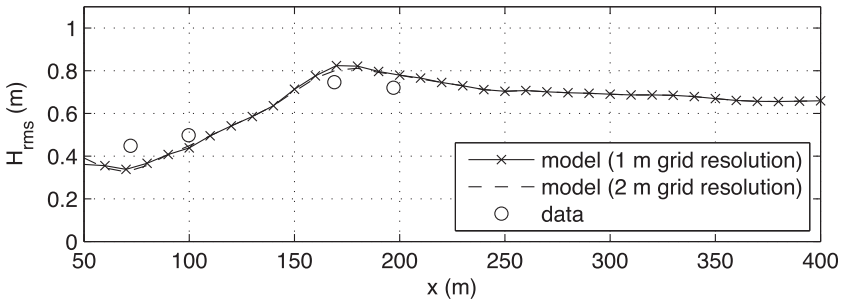

Fig. 16. Comparison of H_{rms} between data (circles) and model (solid-cross line) at $y = 65$ m as a function of cross-shore location.

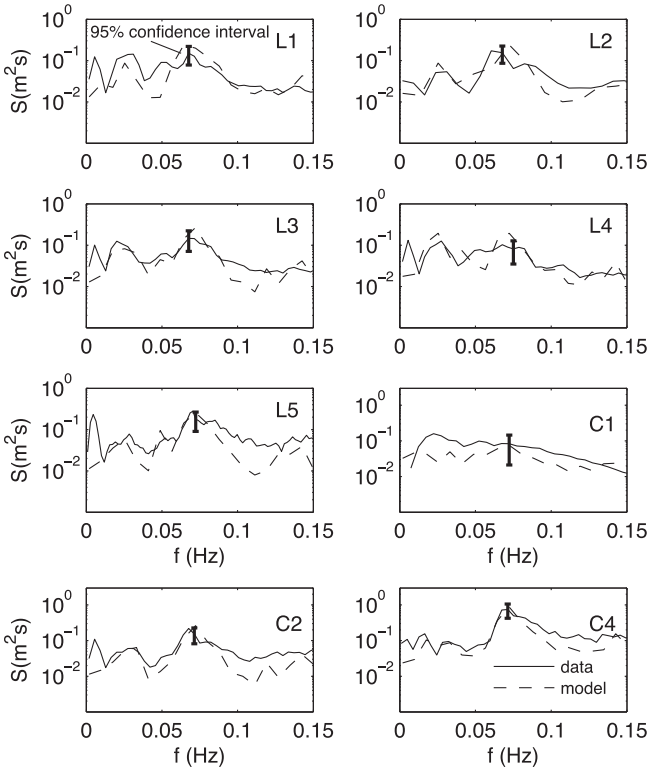

Fig. 17. Comparison of surface elevation spectra at wave gages of the alongshore array (L1–L5) and the cross-shore array (C1,C2 and C4).

with RMSE of 16.4%, 12.3%, 10.5% and 11.4%, respectively, for C1, C2, C4 and C5. In consideration of the lower resolution (2 m × 2 m) used in Geiman et al., we have also run the present example using 2 m × 2 m grid resolution in the present model. The difference in wave height prediction between the two models with different resolutions is basically minimal as demonstrated in Fig. 16.

In Fig. 17, model and observed wave surface spectra are compared at the alongshore measurement array L1–L5 and the cross-shore array C1,C2 and C4. With a peak frequency around 0.7 Hz, both the model and data show lower harmonics generated in the range from 0.2 Hz to 0.4 Hz. Slight under-predictions of wave spectra are found in all the surfzone gages.

The present model results were found to be essentially similar to the results obtained using the original FUNWAVE in Geiman et al. (2011) and showed a similar agreement with the data, suggesting that the shock-capturing breaking scheme has comparable skill to the artificial eddy viscosity formulation in modeling breaking wave-induced circulation.

5. Conclusions

A new version of the FUNWAVE model was developed based on a more complete set of fully nonlinear Boussinesq equations with the vertical vorticity correction derived by Chen (2006) and a time-varying reference elevation introduced by Kennedy et al. (2001). The equations were reorganized in order to facilitate a hybrid numerical scheme, which includes the third-order Runge–Kutta time-stepping and the MUSCL-TVD scheme up to the fourth-order accuracy within the Riemann solver. Wave breaking is modeled by locally switching to the nonlinear shallow water equations where the Froude number exceeds a certain threshold. The wetting–drying method was implemented to model a moving shoreline, instead of the slot method used in the previous FUNWAVE model. The code was parallelized using MPI with non-blocking communication.

Benchmark tests verified the model's capability in simulating wave shoaling, breaking, and wave-induced nearshore circulation. These suggested the following advantages of the new model versus the previous version of FUNWAVE:

(1) The adaptive time stepping is more efficient in a simulation where the local Froude number varies over a large range. The constant time step used in the previous FUNWAVE version is usually selected on an *ad hoc* basis due to unpredictable supercritical fluid conditions.
(2) The shock capturing scheme is robust not only in the treatment of wave breaking, but also in the suppression of numerical instabilities, especially in modeling wave breaking. No filtering is needed in the present model.
(3) The wetting–drying method is better adapted than the slot method to modeling the swash zone and coastal inundation.

In addition, the model accurately predicted wave runup against a suite of benchmark test data (Tehranirad et al., 2011).

Acknowledgements

This work was supported by the Office of Naval Research, Coastal Geosciences Program Grant N00014-10-1-0088 (Shi and Kirby), and the National Science Foundation, Physical Oceanography Program Grant OCE-0727376 (Kirby and Geiman), and Geophysics Program Grant EAR-09-11499 (Grilli and Harris). Development and testing of the parallel code was carried out on UD's Chimera computer system, supported by NSF award CNS-0958512.

Appendix A. Expansions of $\mathbf{V}_1', \mathbf{V}_1'', \mathbf{V}_2, \mathbf{V}_3$ and $\mathbf{V}_4$

The expanded forms of $(U_1', V_1'), (U_1'', V_1''), (U_2, V_2), (U_3, V_3)$ and (U_4, V_4) can be written as

$$U_1' = \frac{1}{2}(1-\beta)^2h^2(u_{xx}+v_{xy}) - (1-\beta)h[(hu)_{xx}+(hv)_{xy}] - \left[\beta(1-\beta)h\eta - \frac{1}{2}\beta^2\eta^2\right](u_{xx}+v_{xy}) + \beta\eta\left[(hu)_{xx}+(hv)_{xy}\right] - \left\{\frac{\eta^2}{2}(u_x+v_y) + \eta\left[(hu)_x+(hv)_y\right]\right\}_x \quad (46)$$

$$V_1' = \frac{1}{2}(1-\beta)^2h^2(u_{xy}+v_{yy}) - (1-\beta)h\left[(hu)_{xy}+(hv)_{yy}\right] - \left[\beta(1-\beta)h\eta - \frac{1}{2}\beta^2\eta^2\right](u_{xy}+v_{yy}) + \beta\eta\left[(hu)_{xy}+(hv)_{yy}\right] - \left\{\frac{\eta^2}{2}(u_x+v_y) + \eta\left[(hu)_x+(hv)_y\right]\right\}_y \quad (47)$$

$$U_1'' = \{\eta\eta_t(u_x+v_y) + \eta[(hu)x+(hv)_y]\}_x \quad (48)$$

$$V_1'' = \{\eta\eta_t(u_x+v_y) + \eta[(hu)x+(hv)_y]\}_y \quad (49)$$

$$U_2 = \left\{(\beta-1)(h+\eta)[u((hu)_x+(hv)_y)_x + v((hu)_x+(hv)_y)_y] + \left[\frac{1}{2}(1-\beta)^2h^2 - \beta(1-\beta)h\eta + \frac{1}{2}(\beta^2-1)\eta^2\right][u(u_x+v_y)_x + v(u_x+v_y)_y] + \frac{1}{2}[(hu)_x+(hv)_y+\eta(u_x+v_y)]^2\right\}_x \quad (50)$$

$$V_2 = \left\{(\beta-1)(h+\eta)[u((hu)_x+(hv)_y)_x + v((hu)_x+(hv)_y)_y] + \left[\frac{1}{2}(1-\beta)^2h^2 - \beta(1-\beta)h\eta + \frac{1}{2}(\beta^2-1)\eta^2\right][u(u_x+v_y)_x + v(u_x+v_y)_y] + \frac{1}{2}[(hu)_x+(hv)_y+\eta(u_x+v_y)]^2\right\}_y \quad (51)$$

$$U_3 = -v\omega_1 - \omega_0\left\{\left[\left(\beta-\frac{1}{2}\right)(h+\eta)\right]\left[(hu)_x+(hv)_y\right]_y + \left[\left(\frac{1}{3}-\beta+\frac{1}{2}\beta^2\right)h^2 + \left(\frac{1}{6}-\beta+\beta^2\right)\eta h + \left(\frac{1}{2}\beta^2-\frac{1}{6}\right)\eta^2\right](u_x+v_y)_y\right\} \quad (52)$$

$$V_3 = -v\omega_1 - \omega_0\left\{\left[\left(\beta-\frac{1}{2}\right)(h+\eta)\right]\left[(hu)_x+(hv)_y\right]_x + \left[\left(\frac{1}{3}-\beta+\frac{1}{2}\beta^2\right)h^2 + \left(\frac{1}{6}-\beta+\beta^2\right)\eta h + \left(\frac{1}{2}\beta^2-\frac{1}{6}\right)\eta^2\right](u_x+v_y)_x\right\} \quad (53)$$

where

$$\omega_0 = v_x - u_y \quad (54)$$

$$\omega_1 = (1-\beta)h_x\{[(hu)_x+(hv)_y]_y + b_2h(u_x+v_y)_y\} - (1-\beta)h_y\{[(hu)_x+(hv)_y]_x + b_2h(u_x+v_y)_x\} \quad (55)$$

$$U_4 = \left(\frac{1}{3}-\beta+\frac{1}{2}\beta^2\right)h^2(u_{xx}+v_{xy}) + \left(\beta-\frac{1}{2}\right)h[(hu)_{xx}+(hv)_{xy}] + \left\{\left[\left(\frac{1}{6}-\beta+\beta^2\right)h\eta + \left(\frac{1}{2}\beta^2-\frac{1}{6}\right)\eta^2\right](u_{xx}+v_{xy}) + \left(\beta-\frac{1}{2}\right)\eta[(hu)_{xx}+(hv)_{xy}]\right\} \quad (56)$$

$$V_4 = \left(\frac{1}{3}-\beta+\frac{1}{2}\beta^2\right)h^2(u_{xy}+v_{yy}) + a_2h[(hu)_{xy}+(hv)_{yy}] + \left\{\left[\left(\frac{1}{6}-\beta+\beta^2\right)h\eta + \left(\frac{1}{2}\beta^2-\frac{1}{6}\right)\eta^2\right](u_{xy}+v_{yy}) + \left(\beta-\frac{1}{2}\right)\eta\left[(hu)_{xy}+(hv)_{yy}\right]\right\} \quad (57)$$

References

Agnon, Y., Madsen, P.A., Schäffer, H.A., 1999. A new approach to high-order Boussinesq models. J. Fluid Mech. 399, 319–333.

Brown, J., MacMahan, J., Reniers, A.J.H.M., Thornton, E., 2009. Surf zone diffusivity on a rip-channeled beach. J. Geophys. Res. 114, C11015. doi:10.1029/2008JC005158.

Chen, Q., 2006. Fully nonlinear Boussinesq-type equations for waves and currents over porous beds. J. Eng. Mech. 132, 220–230.

Chen, Q., Dalrymple, R.A., Kirby, J.T., Kennedy, A.B., Haller, M.C., 1999. Boussinesq modelling of a rip current system. J. Geophys. Res. 104, 20617–20637.

Chen, Q., Kirby, J.T., Dalrymple, R.A., Kennedy, A.B., Chawla, A., 2000. Boussinesq modeling of wave transformation, breaking and runup. II: 2D. J. Waterway Port Coastal Ocean Eng. 126, 48–56.

Chen, Q., Kirby, J.T., Dalrymple, R.A., Shi, F., Thornton, E.B., 2003. Boussinesq modeling of longshore currents. J. Geophys. Res. 108 (C11), 3362. doi:10.1029/2002JC001308.

Erduran, K.S., Ilic, S., Kutija, V., 2005. Hybrid finite-volume finite-difference scheme for the solution of Boussinesq equations. Int. J. Numer. Methods Fluids 49, 1213–1232.

Feddersen, F., Clark, D.B., Guza, R.T., 2011. Modeling surfzone tracer plumes, Part 1: waves, mean currents, and low-freqency eddies. J. Geophys. Res. 116, C11027. doi:10.1029/2011JC007210.

Geiman, J.D., Kirby, J.T., Reniers, A.J.H.M., MacMahan, J.H., 2011. Effects of wave averaging on estimates of fluid mixing in the surf zone. J. Geophys. Res. 116, C04006. doi:10.1029/2010JC006678.

Gobbi, M.F., Kirby, J.T., Wei, G., 2000. A fully nonlinear Boussinesq model for surface waves. II. Extension to $O(kh^4)$. J. Fluid Mech. 405, 181–210.

Gottlieb, S., Shu, C.-W., Tadmore, E., 2001. Strong stability-preserving high-order time discretization methods. SIAM Rev. 43 (1), 89–112.

Hansen, J.B., Svendsen, I.A., 1979. Regular waves in shoaling water: Experimental data. Series Paper 21, ISVA, Technical Univ. of Denmark, Denmark.

Johnson, D., Pattiaratchi, C., 2006. Boussinesq modelling of transient rip currents. Coastal Eng. 53, 419–439.

Kennedy, A.B., Chen, Q., Kirby, J.T., Dalrymple, R.A., 2000. Boussinesq modeling of wave transformation, breaking and runup. I: 1D. J. Waterway Port Coastal Ocean Eng. 126, 39–47.

Kennedy, A.B., Kirby, J.T., Chen, Q., Dalrymple, R.A., 2001. Boussinesq-type equations with improved nonlinear performance. Wave Motion 33, 225–243.

Kim, D.H., Cho, Y.S., Kim, H.J., 2008. Well balanced scheme between flux and source terms for computation of shallow-water equations over irregular bathymetry. J. Eng. Mech. 134, 277–290.

Kim, D.H., Lynett, P.J., Socolofsky, S.A., 2009. A depth-integrated model for weakly dispersive, turbulent, and rotational fluid flows. Ocean Model. 27, 198–214.

Kirby, J.T., Wei, G., Chen, Q., Kennedy, A.B., Dalrymple, R.A., 1998. FUNWAVE 1.0, Fully nonlinear Boussinesq wave model. Documentation and user's manual. Research Report CACR-98-06, Center for Applied Coastal Research, Department of Civil and Environmental Engineering, University of Delaware.

Liang, Q., Marche, F., 2009. Numerical resolution of well-balanced shallow water equations with complex source terms. Adv. Water Res. 32, 873–884.

Lynett, P.J., Liu, P.L.F., 2004. A two-layer approach to wave modelling. Proc. Roy. Soc. London A 460, 2637–2669.

Lynett, P.J., Swigler, D., Son, S., Bryant, D., Socolofsky, S., 2010. Experimental study of solitary wave evolution over a 3D shallow shelf. In: Proceedings of the 32nd International Conference on Coastal Engineering, ASCE, Shanghai, Paper No. 32.

MacMahan, J., Brown, J., Brown, J., Thornton, E., Reniers, A., Stanton, T., Henriquez, M., Gallagher, E., Morrison, J., Austin, M.J., Scott, T.M., Senechal, N., 2010. Mean Lagrangian flow behavior on open coast rip-channeled beaches: new perspectives. Mar. Geol. 268, 1–15.

Madsen, P.A., Murray, R., Sørensen, O.R., 1991. A new form of the Boussinesq equations with improved linear dispersion characteristics. Coastal Eng. 15, 371–388.

Mase, H., Kirby, J.T., 1992. Hybrid frequency-domain KdV equation for random wave transformation. In: Proceedings of the 23rd Internatinal Conference on Coastal Engineering, ASCE, New York, pp. 474–487.

Naik, N.H., Naik, V.K., Nicoules, M., 1993. Parallelization of a class of implicit finite difference schemes in computational fluid dynamics. Int. J. High Speed Comput. 5, 1–50.

Nwogu, O., 1993. An alternative form of the Boussinesq equations for nearshore wave propagation. J. Waterway Port Coastal Ocean Eng. 119, 618–638.

Nwogu, O., Demirbilek, Z., 2001. BOUSS-2D: A Boussinesq wave model for coastal regions and harbors. ERDC/CHL TR-01-25, Coastal and Hydraulics Laboratory, USACOE Engineer Research and Development Center, Vicksburg, MS.

Roeber, V., Cheung, K.F., Kobayashi, M.H., 2010. Shock-capturing Boussinesq-type model for nearshore wave processes. Coastal Eng. 57, 407–423.
Rogers, B.D., Borthwick, A.G.L., Taylor, P.H., 2003. Mathematical balancing of flux gradient and source terms prior to using Roe's approximate Riemann solver. J. Comput. Phys. 192, 422–451.
Shiach, J.B., Mingham, C.G., 2009. A temporally second-order accurate Godunov-type scheme for solving the extended Boussinesq equations. Coastal Eng. 56, 32–45.
Shi, F., Dalrymple, R.A., Kirby, J.T., Chen, Q., Kennedy, A., 2001. A fully nonlinear Boussinesq model in generalized curvilinear coordinates. Coastal Eng. 42, 337–358.
Shi, F., Kirby, J.T., Tehranirad, B., Harris, J.C., 2011. FUNWAVE-TVD, documentation and users' manual. Research Report, CACR-11-04, University of Delaware, Newark, Delaware.
Smagorinsky, J., 1963. General circulation experiments with the primitive equations. I. The basic experiment. Mon. Weather Rev 91, 99–165.
Tehranirad, B., Shi, F., Kirby, J.T., Harris, J.C., Grilli, S., 2011. Tsunami benchmark results for fully nonlinear Boussinesq wave model FUNWAVE-TVD, Version 1.0. Research Report No. CACR-11-02, Center for Applied Coastal Research, University of Delaware.
Tonelli, M., Petti, M., 2009. Hybrid finite volume-finite difference scheme for 2DH improved Boussinesq equations. Coastal Eng. 56, 609–620.
Tonelli, M., Petti, M., 2010. Finite volume scheme for the solution of 2D extended Boussinesq equations in the surf zone. Ocean Eng. 37, 567–582.
Toro, E.F., 2009. Riemann solvers and numerical methods for fluid dynamics: a practical introduction, third ed. Springer, New York.
Wei, G., 1997. Simulation of water waves by Boussinesq models. Ph.D. dissertation, University of Delaware, 202 pp.
Wei, G., Kirby, J.T., 1995. A time-dependent numerical code for extended Boussinesq equations. J. Waterway Port Coastal Ocean Eng. 120, 251–261.
Wei, G., Kirby, J.T., Grilli, S.T., Subramanya, R., 1995. A fully nonlinear Boussinesq model for surface waves: Part I. Highly nonlinear unsteady waves. J. Fluid Mech. 294, 71–92.
Wei, G., Kirby, J.T., Sinha, A., 1999. Generation of waves in Boussinesq models using a source function method. Coastal Eng. 36, 271–299.
Yamamoto, S., Daiguji, H., 1993. Higher-order-accurate upwind schemes for solving the compressible Euler and Navier–Stokes equations. Comput. Fluids 22, 259–270.
Yamamoto, S., Kano, S., Daiguji, H., 1998. An efficient CFD approach for simulating unsteady hypersonic shock-shock interference flows. Comput. Fluids 27, 571–580.
Zelt, J.A., 1991. The runup of nonbreaking and breaking solitary waves. Coastal Eng. 15, 205–246.
Zhen, F., 2004. On the numerical properties of staggered vs. non-staggered grid schemes for a Boussinesq equation model. MCE Thesis, Department of Civil and Environmental Engineering, University of Delaware.
Zhou, J.G., Causon, D.M., Mingham, C.G., Ingram, D.M., 2001. The surface gradient method for the treatment of source terms in the shallow-water equations. J. Comput. Phys. 168, 1–25.